The influence of Southern Ocean winds on the North Atlantic carbon sink

Ben Bronselaer[1], Laure Zanna[1], David R. Munday[1,2], and Jason Lowe[3]

[1]Atmospheric, Oceanic and Planetary Physics, Department of Physics, University of Oxford, Oxford, UK, [2]British Antarctic Survey, Cambridge, UK, [3]Met Office Hadley Centre, Exeter, UK

Abstract   Observed and predicted increases in Southern Ocean winds are thought to upwell deep ocean carbon and increase atmospheric CO_2. However, Southern Ocean dynamics affect biogeochemistry and circulation pathways on a global scale. Using idealized Massachusetts Institute of Technology General Circulation Model (MITgcm) simulations, we demonstrate that an increase in Southern Ocean winds reduces the carbon sink in the North Atlantic subpolar gyre. The increase in atmospheric CO_2 due to the reduction of the North Atlantic carbon sink is shown to be of the same magnitude as the increase in atmospheric CO_2 due to Southern Ocean outgassing. The mechanism can be described as follows: The increase in Southern Ocean winds leads to an increase in upper ocean northward nutrient transport. Biological productivity is therefore enhanced in the tropics, which alters the chemistry of the subthermocline waters that are ultimately upwelled in the subpolar gyre. The results demonstrate the influence of Southern Ocean winds on the North Atlantic carbon sink and show that the effect of Southern Ocean winds on atmospheric CO_2 is likely twice as large as previously thought in past, present, and future climates.

1. Introduction

Paleoproxy and historical data show large changes in atmospheric pCO_2, indicating variations in the atmosphere-ocean exchange of carbon. Changes in atmospheric forcing, such as Southern Hemisphere westerly wind stress, can have a strong influence on the carbon cycle. The impact of observed and projected Southern Ocean wind increase [*Swart et al.*, 2014; *Bracegirdle et al.*, 2013] on the Southern Ocean carbon flux has been extensively studied [e.g., *Le Quere et al.*, 2007; *Lovenduski et al.*, 2008; *Lovenduski and Ito*, 2009; *Ito et al.*, 2010; *Lauderdale et al.*, 2013; *Munday et al.*, 2014]. Increased Southern Ocean winds are thought to increase upwelling of deep ocean natural carbon, elevating local ocean pCO_2. The elevated ocean pCO_2 leads to a reduction in local sink of anthropogenic CO_2 and a subsequent increase in atmospheric CO_2 levels.

However, little attention has gone into estimating the climate impacts of dynamical and biogeochemical changes induced by the Southern Ocean wind stress outside of the Southern Ocean. The Southern Ocean circulation forms part of the global meridional overturning circulation [*Gnanadesikan*, 1999; *Marshall and Speer*, 2012] and has a strong influence on transport pathways [*Ito et al.*, 2010; *Palter et al.*, 2010], including in the North Atlantic. Southern Ocean winds act to ventilate the deep ocean, which is richer in nutrients than the surface ocean. The wind-driven ventilation in the Southern Ocean mixes nutrients into the surface ocean, giving it a large effect on ocean biogeochemistry and biological productivity on a global scale [*Marinov et al.*, 2006]. *Anderson et al.* [2002] and *Sarmiento et al.* [2004] show that increased Southern Ocean upwelling increases nutrient supply north of the Southern Ocean and enhances high- and low-latitude biological productivity. Changes induced in the Southern Ocean can therefore have far-reaching impact on ocean dynamical and biogeochemical properties.

Studies such as *Lauderdale et al.* [2013] examine the basin-scale response to Southern Ocean wind stress perturbations on the dynamics and distribution of carbon but focus on the local contribution of wind stress on atmospheric pCO_2. The nonlocal effect of the Southern Ocean winds on atmospheric CO_2, via change in global-scale transport pathways and in nutrient export from the Southern Ocean, remains to be estimated. We focus primarily on understanding the response of other major carbon sinks to changes induced in the Southern Ocean.

In the Atlantic, the major oceanic sink of atmospheric carbon (both natural and anthropogenic) is the subpolar gyre [*Group*, 1998; *Dickson et al.*, 2008; *Khatiwala et al.*, 2009; *Kieke and Yashayaev*, 2014]. Any changes in
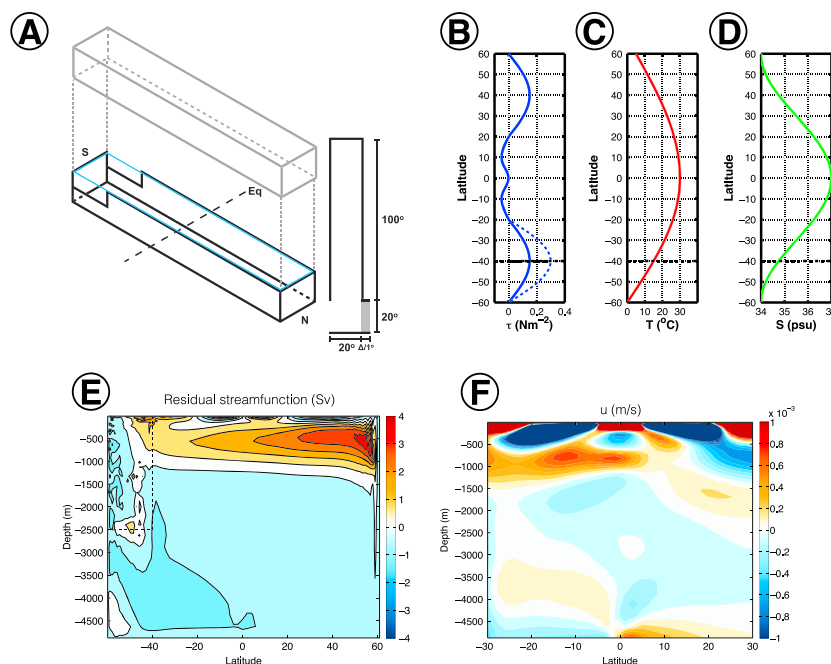
Figure 1. (a) Schematic of MITgcm sector. Latitudinal profiles of surface boundary conditions for the control experiment of (b) wind, with the dashed line showing a $2 \times \tau_{SO}$ perturbation, (c) temperature, and (d) salinity. Control experiment steady state (e) residual overturning stream function and (f) zonal mean velocity.

the North Atlantic ocean carbon chemistry will therefore greatly impact the magnitude of the local carbon sink and subsequently alter atmospheric CO_2 levels. *Halloran et al.* [2015], for example, show that the biogeochemical properties of the subpolar gyre are affected by the water advected from the tropics and Southern Ocean. Southern Ocean winds have the potential to influence the North Atlantic carbon sink by affecting the biogeochemical properties of the waters advected from the Southern Ocean to the North Atlantic.

The aim of this paper is to assess the nonlocal effect of Southern Ocean winds on atmospheric CO_2 and to demonstrate that increased Southern Ocean winds affect the North Atlantic pCO_2 through a novel mechanism. The mechanism can be summarized as follows: increased Southern Ocean wind stress enhances nutrient transport toward the tropics, thereby increasing tropical biological productivity. This in turn affects the chemistry of underlying subthermocline waters. The tropical subthermocline waters are subsequently advected to the North Atlantic subpolar gyre by equatorial currents and the meridional overturning circulation (MOC), reducing the capacity of the subpolar gyre to absorb atmospheric CO_2.

The paper is structured as follows. We provide a description of the model used in this paper in section 2, with details regarding the model design and mean state. Section 3 describes and quantifies the effect of Southern Ocean wind perturbations on the North Atlantic carbon sink. The subsequent section 4 will detail the key steps in the mechanism, and section 5 summarizes the main conclusion, caveats, and implications of the presented study.

2. Model Design and Control Experiment

To study the effect of Southern Ocean winds on the North Atlantic carbon sink, we use the Massachusetts Institute of Technology General Circulation Model (MITgcm) [*Marshall et al.*, 1997] in an idealized configuration designed to mimic the Atlantic and Southern Oceans. The setup and parameters are similar to *Munday et al.* [2014] at $2° \times 2°$ horizontal grid spacing with eddies parametrized using the Gent-McWilliams [*Gent and McWilliams*, 1990] scheme with a constant coefficient. The domain, shown in Figure 1a, is a sector 20° wide in longitude, extending to 60°N/S with a reentrant channel between 60° and 40°S to allow for a circumpolar current. The basin is 5000m deep, except at the channel boundaries where a 2500m deep sill represents Drake Passage. Coupled to the ocean, there is a well-mixed atmospheric box which only solves for atmospheric pCO_2, and the air-sea flux of carbon is parametrized following *Wanninkhof* [1992]. The model resolution is
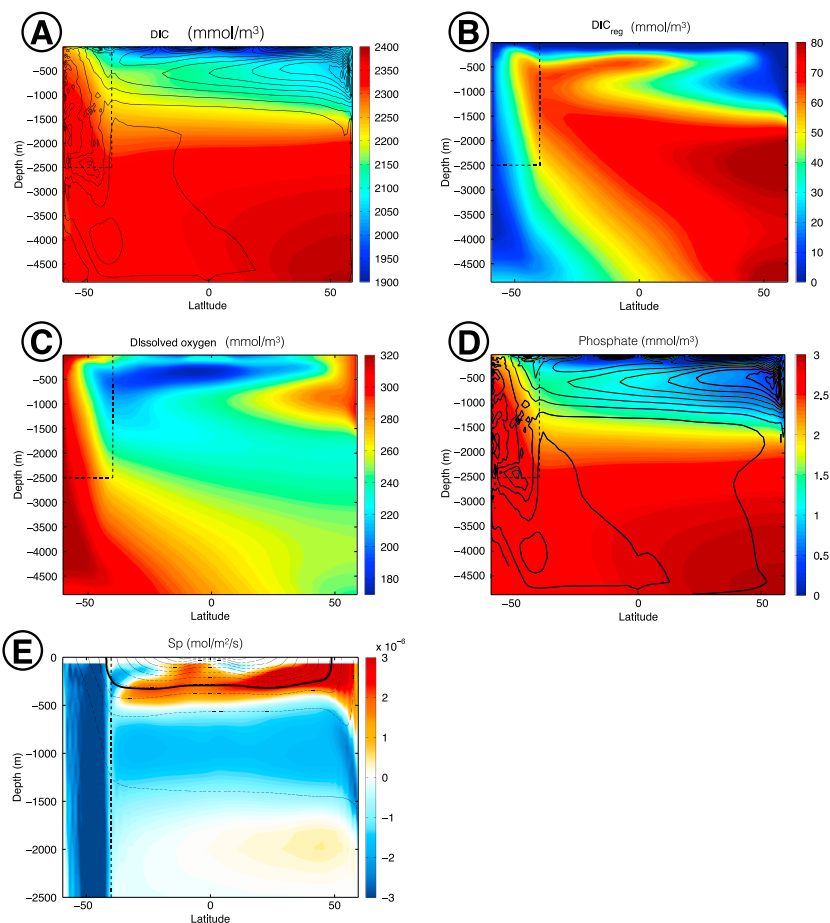
Figure 2. Zonally averaged (a) total dissolved inorganic carbon, (b) regenerated dissolved inorganic carbon, (c) dissolved oxygen, and (d) dissolved phosphate. Dashed black lines in Figures 2a–2d indicate the extent of the channel, and the solid black lines are residual overturning stream function contours spaced 1Sv (sverdrup, 10^6 m^3/s) apart. (e) Zonally averaged meridional nutrient stream as defined by equation (5), with dashed lines showing surfaces of constant density and the thick black line showing the $\sigma_\theta = 26$ kg/m^3 density surface.

chosen such that a large set of perturbation experiments can be run for centuries while still capturing the main features of a large-scale circulation and the appropriate response of the ocean carbon cycle. Such a setup is widely used to conduct large-scale ocean studies [e.g., *Wolfe and Cessi*, 2010; *Ito and Follows*, 2003; *Munday et al.*, 2013].

The model is forced with a zonal wind stress profile shown in Figure 1b with $\overline{\tau_{SO}} = 0.13$ N/m^2 (where the subscipt "SO" indicates the Southern Ocean between 60° and 40°S and the overline indicates a spatial average). Heat and freshwater fluxes are prescribed through temperature and salinity restoring profiles (Figures 1c and 1d), which broadly match the observed distributions in the Atlantic. The resulting residual (sum of Eulerian and eddy) overturning stream function is shown in Figure 1e [*Marshall and Radko*, 2003].

The model also supports a series of equatorial and midlatitude zonal currents, with a westward equatorial current, an eastward undercurrent [*Knauss*, 1960; *Philander*, 1973; *Wyrtki and Kilonsky*, 1984; *Philander et al.*, 1987], and a series of stationary eastward jets on either side of the equator [*Tsuchiya*, 1972; *Firing et al.*, 1998; *Rowe et al.*, 2000; *Izumo et al.*, 2002; *Qiu et al.*, 2013] (Figure 1f). While the structures are similar to observations, the magnitude of the currents in the MITgcm are smaller, likely due to the model geometry and its coarse horizontal and vertical resolution. The equatorial jets, alongside vertical and horizontal mixing, are important factors for ventilation of the shadow zone [*Brandt et al.*, 2015]: a region of the subsurface ocean that is unventilated by the wind-driven gyre circulation.

The ocean model contains a biogeochemical component with seven tracers: dissolved inorganic carbon (DIC), alkalinity, preformed alkalinity, phosphate, preformed phosphate, dissolved organic phosphorous, and
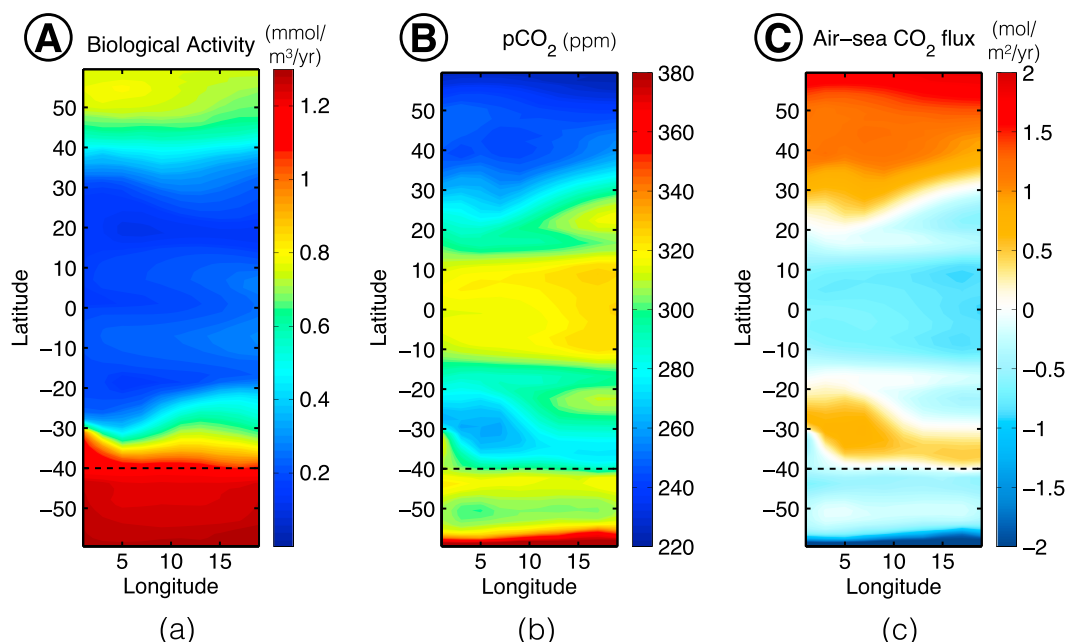
Figure 3. Steady state biogeochemical quantities in the control experiment: (a) Mixed layer average biological activity (mmol/m^3/year of phosphate), (b) mixed layer ocean pCO$_2$, and (c) air-sea CO$_2$ flux. Dashed black lines indicate the extent of the channel.

dissolved oxygen [*Dutkiewicz et al.*, 2008; *Follows et al.*, 2006]. Biological productivity is governed by phosphate and light limitation. Figures 2a–2c show the zonally averaged distribution of DIC, regenerated DIC, and dissolved oxygen. The maximum in DIC concentration is located in the abyssal cell at high latitudes where water is oldest. Regenerated DIC concentrations are generally high where dissolved oxygen concentrations are low since oxygen is used up in the remineralization of soft organic matter. The upper ocean distributions of DIC and alkalinity are in agreement with Global Data Analysis Project (GLODAP) climatology [*Key et al.*, 2004].

The model shows the presence of an oxygen-minimum zone (OMZ) in the shadow zone between 100 and 1000 m depth, with corresponding high regenerated carbon concentrations. The lack of wind-driven ventilation in the shadow zone leads to a buildup of organic carbon and the associated removal of dissolved oxygen. The meridional and vertical extent of the OMZ compares well with other studies such as *Ito and Follows* [2005], although the magnitude is slightly higher in the presented model compared to other studies. For a more detailed description of the distribution of biogeochemical tracers in the model, see *Munday et al.* [2014].

Mixed layer biological activity is shown in Figure 3a, with higher activity at high latitudes than at the equator and little biological activity in the oligotrophic subtropical regions. Such patterns are supported by satellite chlorophyll observations and other models [*Williams and Follows*, 2011]. The efficiency of the biological pump in the model (given by the ratio of mixed layer nutrient concentration over the nutrient concentration at 100–200 m depth), at high latitudes is 0.1–0.2, while in the tropics it is between 0.6 and 0.8. These numbers are consistent with observations [*Sarmiento et al.*, 2004]. The spatial pattern, including the large-scale meridional gradients of pCO$_2$, shown in Figure 3b, is comparable to observations [*Takahashi et al.*, 2009; *Valsala and Maksyutov*, 2010]. As a result, there is a positive air-sea flux of carbon north of the southern channel and in the northern subpolar region (40°–60°N) and a negative air-sea flux of carbon in the southern channel and tropics, again consistent with observations [*Takahashi et al.*, 2009] (Figure 3c). Overall, the large-scale distribution and magnitude of the biogeochemical tracers agrees well with other studies [e.g., *Ito and Follows*, 2005] and observations [*Feely et al.*, 2001; *Gruber*, 1998].

3. The Response of the North Atlantic Carbon Sink to Increased Southern Ocean Wind Stress

3.1. The North Atlantic Carbon Flux

To examine the response of the carbon system to Southern Ocean wind stress perturbations, the wind stress between 60° and 20°S, τ_{SO}, is multiplied by a constant in a set of numerical experiments (see Figure 1b).
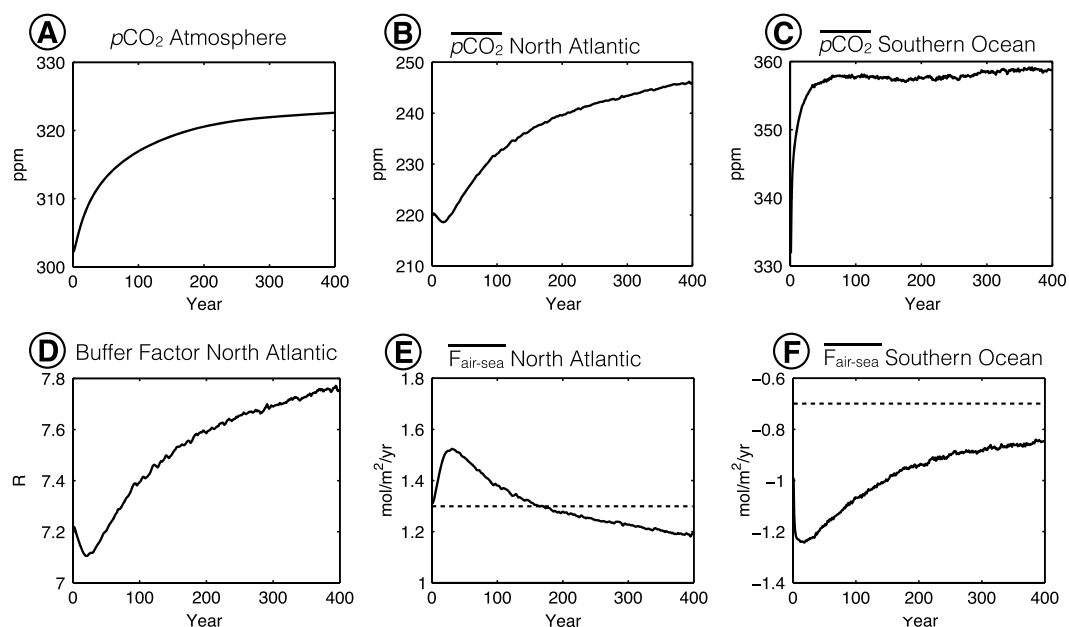
Figure 4. Time evolution of (a) Southern Ocean mean surface pCO_2^o, (b) North Atlantic subpolar gyre mean surface pCO_2^o, (c) atmospheric pCO_2^a, (d) North Atlantic mean surface Revelle buffer factor, and (e) North Atlantic and (f) Southern Ocean net air-sea flux of carbon, in the $2 \times \tau_{SO}$ experiment. The dashed lines in Figures 4e and 4f show the control mean air-sea flux. The overline indicates a spatial mean between 40°–60°N and 40°–60°S for the North Atlantic and Southern Oceans, respectively.

Each perturbed experiment is run for 400 years, after which time the dynamics of the upper 1000m has fully equilibrated. We will examine the carbon cycle response to a range of wind stress perturbations, while specific examples will be drawn from the $2 \times \tau_{SO}$ scenario. The $2 \times \tau_{SO}$ experiment was run for 3000 years to verify that the results are not dependent on the length of integration. The response of the circulation to changes in Southern Ocean wind is linear. The Ekman transport and strength of the upper overturning cell increase linearly with wind stress. Our results therefore scale with forcing scenarios without nonlinear behavior.

Figure 4 illustrates the impact of ocean pCO_2, pCO_2^o, in the North Atlantic subpolar gyre on atmospheric pCO_2, pCO_2^a. Figure 4 shows time series of atmospheric pCO_2 (Figure 4a), the area-averaged ocean pCO_2 for the North Atlantic subpolar gyre (40°–60°N, Figure 4b), and the Southern Ocean (40°–60°S, Figure 4c) in the $2 \times \tau_{SO}$ wind stress perturbation experiment. The initial adjustment of the Southern Ocean pCO_2^o occurs within the first few decades. The atmospheric pCO_2 shows an initial increase over a few decades which coincides with the time scale of the local response of the Southern Ocean pCO_2^o. However, the short-term response is followed by a long-term centennial adjustment in pCO_2^a due to the perturbed ocean carbon reservoir in the North Atlantic. We refer to the atmospheric pCO_2^a anomalies induced by the North Atlantic subpolar gyre as the nonlocal effect, with a time scale set by the adjustment of the North Atlantic subpolar gyre pCO_2^o.

The increase in North Atlantic pCO_2^o shown in Figure 4b depends on the adjustment of the mean surface Revelle buffer factor R (Figure 4d) [*Revelle and Suess*, 1957]. R measures the fractional ocean pCO_2 change (denoted by δ) given a fractional change in DIC and vice versa such that

$$R = \frac{\delta pCO_2}{pCO_2} / \frac{\delta DIC}{DIC} \approx \frac{2 - Alk/DIC}{Alk/DIC - 1}, \tag{1}$$

where Alk is the alkalinity. The buffer factor R quantifies the amount of carbon that can be stored in the form of DIC for a given change in atmospheric CO_2 concentration. High buffer factor systems are able to absorb changes in ocean pCO_2 by storing carbon in the form of DIC. For example, in a high buffer factor region which absorbs atmospheric carbon, local DIC does not change significantly. Therefore, more carbon remains in the form of dissolved CO_2, leading to higher pCO_2^o values and less uptake of atmospheric CO_2. The value of R can be approximated in terms of the ratio of alkalinity over DIC, as shown in equation (1). As alkalinity levels increase, the buffer factor decreases and the ocean becomes more capable of absorbing atmospheric CO_2 anomalies. Conversely, increasing DIC concentrations reduce the ocean's capacity to buffer atmospheric CO_2 changes.

Figure 4d shows that the temporal evolution of North Atlantic R corresponds to the change in North Atlantic pCO_2 shown in Figure 4b. Changes in the buffer factor account for 94% of the change in North Atlantic pCO_2, while other changes such as temperature and salinity account for the remainder (using the approach of *Lovenduski et al.* [2007]). As a result of the increase in North Atlantic pCO_2, the yearly air-sea flux of carbon in the region, $\overline{F_{\text{air-sea}}}$, is reduced compared to that of the control run (Figure 4e). After roughly 425 years of the wind stress perturbation, the cumulative flux perturbation in the North Atlantic subpolar region becomes zero such that the North Atlantic subpolar region becomes a net emitter of carbon relative to the control state. The increase in Southern Ocean wind therefore induces a reduction in the North Atlantic carbon sink. The air-sea carbon flux in the Southern Ocean (Figure 4f) also shows a long-term decrease due to slow buildup of atmospheric CO_2 driven by the North Atlantic, since the Southern Ocean pCO_2 remains constant after 100 years of wind stress perturbation. After 400 years, the net change in the North Atlantic carbon flux is comparable in magnitude to the change in the Southern Ocean carbon flux.

3.2. Relative Feedback of the North Atlantic on Atmospheric CO_2

To quantify the strength of the nonlocal climate feedback on atmospheric pCO_2 due to Southern Ocean wind stress, we compare it with the change in atmospheric CO_2 due to Southern Ocean outgassing, i.e., the local feedback. We define the nonlocal feedback parameter ϵ which relates a change in Southern Ocean pCO_2^o, $\Delta \overline{pCO_{2SO}^o}$, to the subsequent change in North Atlantic pCO_2, $\Delta \overline{pCO_{2NA}^o}$. If the pCO_2^o in the Southern Ocean is altered through changes in the large-scale circulation and biogeochemistry, the perturbed ocean dynamical and biogeochemical state will also cause changes in the pCO_2 elsewhere, such as in the North Atlantic (as shown in Figure 4). The relative changes in pCO_2, $\Delta \overline{pCO_{2SO}^o}$, and $\Delta \overline{pCO_{2NA}^o}$ will therefore be related to one another:

$$\Delta \overline{pCO_{2NA}^o} = \epsilon \Delta \overline{pCO_{2SO}^o}. \tag{2}$$

We can use ϵ to express the atmospheric pCO_2 anomaly, ΔpCO_2^a, due to a change in Southern Ocean pCO_2^o, by considering the air-sea flux of carbon $F_{\text{air-sea}}$ over the global ocean. The air-sea flux equation takes the following form [*Wanninkhof*, 1992]:

$$F_{\text{air-sea}} = k \left(pCO_2^a - pCO_2^o \right), \tag{3}$$

where k is the gas transfer velocity. We integrate equation (3) over the global ocean. At equilibrium, the net air-sea flux is zero such that $\int F_{\text{air-sea}} dA = 0$. However, we split the integral into three different regions: the Southern Ocean, the North Atlantic subpolar gyre, and the rest of the ocean basin, denoted by the subscripts SO, NA, and E, respectively. By considering a perturbation in atmospheric pCO_2, ΔpCO_2^a, we can then write

$$\Delta pCO_2^a = (1 + \epsilon \frac{P_{NA}}{P_{SO}}) P_{SO} \Delta \overline{pCO_{2SO}^o} + \Delta P_{SO} \overline{pCO_{2SO}^o} + \Delta P_{NA} \overline{pCO_{2NA}^o} + \Delta P_E \overline{pCO_{2E}^o}, \tag{4}$$

where P_{SO}, P_{NA}, and P_E are the area fractions of the respective regions, weighted by the local wind stress (see supporting information). The first term in equation (4) is the change in atmospheric pCO_2 due to changes in the ocean pCO_2. In the case of $\epsilon = 0$, there would be no nonlocal effect and the change in atmospheric pCO_2 would be due to change in Southern Ocean pCO_2 alone. If ϵ is positive and takes a value of 1, the net feedback is positive and doubles the local Southern Ocean feedback on atmospheric pCO_2, since P_{SO} and P_{NA} are roughly of equal magnitude. Conversely, if ϵ is negative with a value of -1, there would be an opposing nonlocal feedback which cancels out the local effect of the Southern Ocean wind stress. The second, third, and fourth terms in equation (4) quantify the change in atmospheric pCO_2 due to the enhanced turbulent air-sea transfer of CO_2. However, these terms mostly cancel each other out and only account for 5–10% of the total ΔpCO_2^a.

The value of ϵ can be estimated using both equations (2) and (4), since all terms apart from ϵ can be calculated and diagnosed from the MITgcm simulations. The results of the calculations are shown in Figure 5. While there are differences in the results between using equations (2) and (4), the order of magnitude and trend of the calculated values of ϵ are similar. Values of ϵ are positive and range between 0.5 and 0.9 for weak wind stress perturbations. The magnitude of ϵ increases as the wind stress increases; ϵ is roughly 1.2 for a doubling of Southern Ocean wind stress. For all experiments, ϵ increases with time (not shown): from less than 0.4 in the first decade after the wind stress perturbation is initially applied to the quasi-equilibrium values of roughly 1
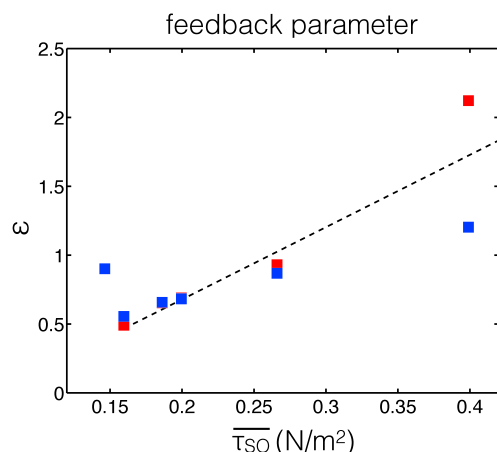
Figure 5. The feedback parameter ϵ as a function of wind stress in MITgcm estimated using equations (2) (blue) and (4) (red). The black line shows the linear trend.

(as shown in Figure 5). The climate feedback of Southern Ocean wind stress on atmospheric pCO$_2$ is therefore almost doubled by the nonlocal effect. To understand the reason behind the change in the North Atlantic carbon sink, the following sections will describe the mechanism by which Southern Ocean winds influence the North Atlantic buffer factor, $\overline{R_{na}}$, and set the long-term centennial adjustment time scale of atmospheric pCO$_2$ anomalies.

4. Southern Ocean Winds, Equatorial Biology, and the North Atlantic Buffer Factor

4.1. The Effect of Southern Ocean Winds on Nutrient Streams

In the Southern Ocean, surface biology is inefficient due to strong light and iron limitation [*Boyd et al.*, 2000; *Coale et al.*, 2004; *DeVries et al.*, 2012] such that the upwelled nutrients remain mostly unused. Instead, the nutrients are transported northward and into the ocean interior following the subsurface currents in what are commonly referred to as nutrient streams [*Pelegri and Csanady*, 1991; *Pelegri et al.*, 1996, 2006; *Williams et al.*, 2006, 2011].

A nutrient stream is an advective pathway through which nutrients are transported from regions of upwelling and nutrient excess, such as the Southern Ocean, to nutrient-poor regions such as the equator and the northern high latitudes (see Figure 2d). The advective pathways mainly follow streamlines of the overturning circulation. Ekman transport drives nutrients northward and out the Southern Ocean [*Williams and Follows*, 1998], where it is subducted below the mixed layer during the formation of Antarctic Intermediate Water. Transport is then predominantly isopycnal, with nutrients gradually reinducted into the mixed layer as isopycnals shoal toward the surface in the North Atlantic subpolar region [*Williams et al.*, 2006]. North of the Southern Ocean where biology is far more efficient, the nutrient stream causes an increase in macronutrient-limited biological productivity [*Sarmiento et al.*, 2004]. The nutrient stream $S_P(x, y, z, t)$ is defined here as the meridional transport of phosphorus, in the form of phosphate PO$_4^{3-}$, by the meridional residual velocity field v and is given by

$$S_P(x, y, z, t) = \left[\text{PO}_4^{3-}\right] v, \qquad (5)$$

where the square brackets indicate concentration. The zonally averaged nutrient stream S_P is shown in Figure 2e for the MITgcm control run.

Physical transport in the ocean interior is mostly adiabatic along isopycnals, so the location of the nutrient stream lies along surfaces of constant density and its strength is modulated by the biological flux of nutrients [*Pelegri et al.*, 1996]. In the current numerical setup, the maximum transport occurs along the potential density surface $\sigma_\theta = 26$ kg/m^3 (σ_{26}), shown in Figure 2e for the control run. Therefore, we interpolate the meridional transport of phosphate onto σ_{26}. Figure 6 shows the meridional nutrient transport, S_P (Figure 6a), the steady state concentration of PO$_4^{3-}$ (Figure 6b) along σ_{26}, and the mean mixed layer biological productivity, F_{bio} (Figure 6c). The spatial pattern of S_P shows the (positive) nutrient stream originating just north of the southern channel where intermediate mode water is formed in region 1. The nutrient stream follows the northward MOC transport along the western boundary in region 2, strengthening until it reaches the northern subpolar gyre, where the nutrients are inducted back into seasonal thermocline in region 3.

The effect of increased Southern Ocean winds on the nutrient transport is shown in Figures 6d–6f after 400 years of the $2 \times \tau_{SO}$ perturbation experiment. Due to the increase in Southern Ocean wind-induced vertical mixing, there is a global increase in concentrations of PO$_4^{3-}$ along the perturbed $\sigma_\theta = 26$ kg/m^3 surface (σ_{26}') in the Southern Hemisphere (Figure 6e). The wind stress perturbation also causes an increase in the meridional velocity v along σ_{26}'. As a result, there is an increase in the northward nutrient stream (Figure 6d). The increase in surface nutrients leads to additional nutrients being introduced into the nutrient-limited equatorial shadow
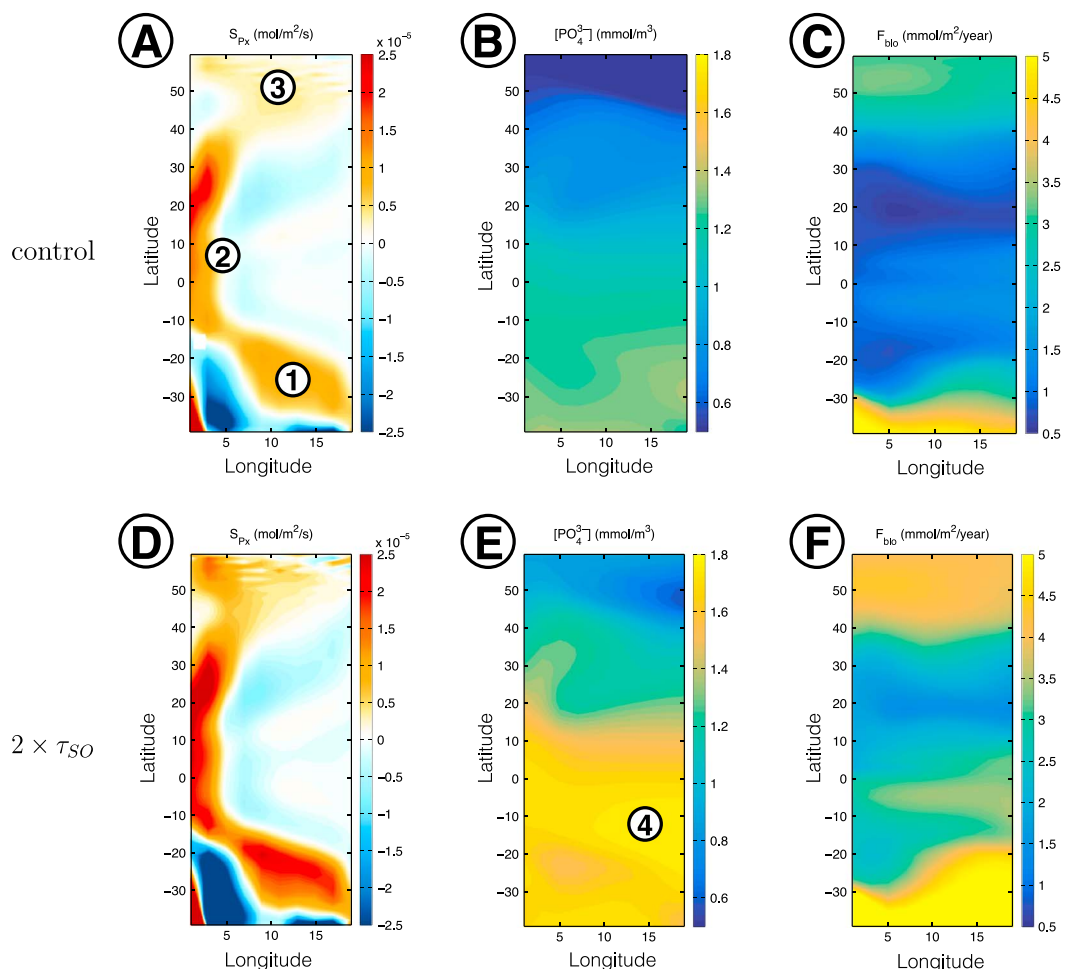
Figure 6. The nutrient stream (a, d) S_p, (b, e) phosphorous on the $\sigma_\theta = 26$ kg/m^3 surface, and (c, f) the mean mixed layer biological productivity. Figures 6a–6c are for the control run, and Figures 6d–6f are after 400 years of a $2 \times \tau_{SO}$ perturbation. Only fields north of the southern channel are shown for clarity.

zone in region 4 via eastward equatorial jets and mixing across the southern shadow zone boundary. Subsequently, mixed layer biological productivity is strongly enhanced north of the southern channel and in the eastern tropics where nutrients are upwelled due to wind stress divergence. For the $2 \times \tau_{SO}$ experiment, the increase in biological productivity is less than 10% in the southern channel, between 20% and 40% in the subpolar gyre, but more than 200% between 20°S and 20°N. In the northern subpolar gyre, the response in biological productivity is not as strong as that in the tropics. This relatively weak response in the subpolar gyre is partly due to high-latitude light limitation [*Nielsdottir et al.*, 2009] and partly due to the depletion of the nutrient stream by the time it reaches the northern end of the basin. Most of the increase in biology is therefore centered around the eastern tropics.

4.2. Surface Biology and the Revelle Buffer Factor

An increase in equatorial biology can reduce atmospheric pCO$_2$ by drawing more carbon from the mixed layer to form biological tissue, therefore reducing ocean surface pCO$_2^o$ and increasing the air-sea flux of carbon into the ocean. Conversely, it can increase atmospheric pCO$_2$ by affecting the chemistry of subthermocline waters in the shadow zone. Surface biology utilizes DIC and alkalinity at different rates. To understand the effect of biology on the buffer factor, let us consider the influence of mixed layer biology on the mixed layer chemistry. The key points discussed below are also summarized in the diagram in Figure 7.

Production of soft matter reduces DIC by 117mol for every mole of phosphate and increases alkalinity by 16mol, following Redfield stoichiometry [*Redfield*, 1934; *Anderson and Sarmiento*, 1994; *Weber and Deutsch*, 2012]. The formation or dissolution of 1mol of calcite (hard tissue), on the other hand, reduces DIC by 1mol and
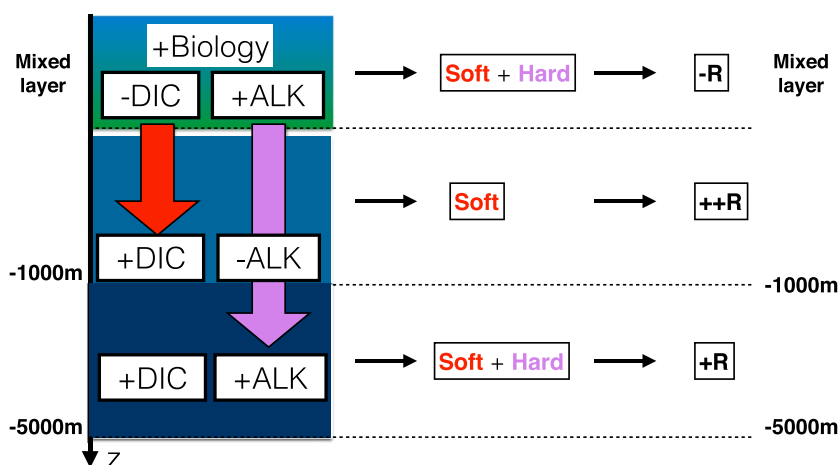
Figure 7. Diagram of the influence of surface biology on the Revelle buffer factor R. As mixed layer biological activity increases, mixed layer DIC is reduced and alkalinity is increased, lowering the buffer factor. Underneath the mixed layer to roughly 1000 m depth, more soft matter is remineralized compared to hard tissue, leading to an increase in DIC and a reduction of alkalinity, resulting in a strong increase in the buffer factor. Deep in the water column, remineralization of soft and hard tissue is comparable giving an increase in both DIC and alkalinity, resulting in a more moderate increase in the buffer factor.

alkalinity by 2mol. Surface biology therefore changes the local concentrations of DIC and Alk depending on the relative export and remineralization of soft matter and calcite. The relative export of hard to soft matter, r, is known as the "rain ratio." Studies of climatological basin-wide and local seasonal data give a rain ratio between 0.05 and 0.1 in the open ocean; the former is used in the MITgcm experiments conducted here [*Sarmiento et al.*, 2002; *Jin et al.*, 2006; *Emerson et al.*, 2011]. For all values of r, an increase in surface biology results in a decrease of the relative ratio of DIC/Alk within the mixed layer.

Surface biology also affects the vertical transport of DIC and alkalinity in the ocean. The soft matter that is produced in the ocean mixed layer falls through the water column until it is remineralized back into DIC, in the form of C_{soft}. The remineralization of soft matter therefore increases DIC and reduces alkalinity. Similarly, calcite shells produced in the mixed layer fall through the water column until they are dissolved into DIC in the form of C_{carb}. Dissolution of calcite increases DIC and alkalinity. The remineralization depth of soft matter is shallower than hard tissue such that just below the mixed layer, remineralization of organic matter is mostly due to soft tissue which increases the relative ratio of DIC to Alk.

The relative concentration of DIC and alkalinity of water parcels, influenced by surface biology, is pivotal for the climate system since they determine the value of the Revelle buffer factor R and therefore the capacity of the ocean to absorb atmospheric CO_2 (equation (1)). In regions of high biological activity, surface waters are reduced in R and the underlying waters are therefore enhanced in R. If these water parcels are then advected away and upwelled at the surface elsewhere, they will increase R in the region of upwelling. Water parcels with an elevated buffer factor R will be less capable of absorbing atmospheric CO_2 anomalies, leading to a local reduction in the ocean carbon sink.

As Southern Ocean winds increase and surface biological productivity is enhanced across the global ocean, the strongest increase in the buffer factor R occurs below the thermocline in the equatorial shadow zone along σ'_{26} (Figure 8), where the largest relative changes in DIC and Alk occur. After 50 years (Figure 8a), there is an increase in R in the southern channel associated with increased upwelling of DIC-rich waters (region 1). A positive R anomaly occurs in the equatorial shadow zone due to the increased biological activity (region 2). After another 100 years (Figure 8b), the anomaly in R in the southern channel has decayed, while the tropical anomaly signal intensified. Because ventilation of the shadow zone is sluggish compared to the rest of the ocean, the increase in the downward flux of organic matter from the surface causes a slow buildup of DIC and a slow reduction of alkalinity in the shadow zone leading to a rise of R anomaly for centuries.

The increase in R generated in the eastern tropics is transported predominantly westward within the shadow zone through the equatorial current, where it is then entrained by the nutrient stream in the western boundary of the shadow zone. As shown in Figure 8d, an additional recirculation of the R anomaly within the shadow
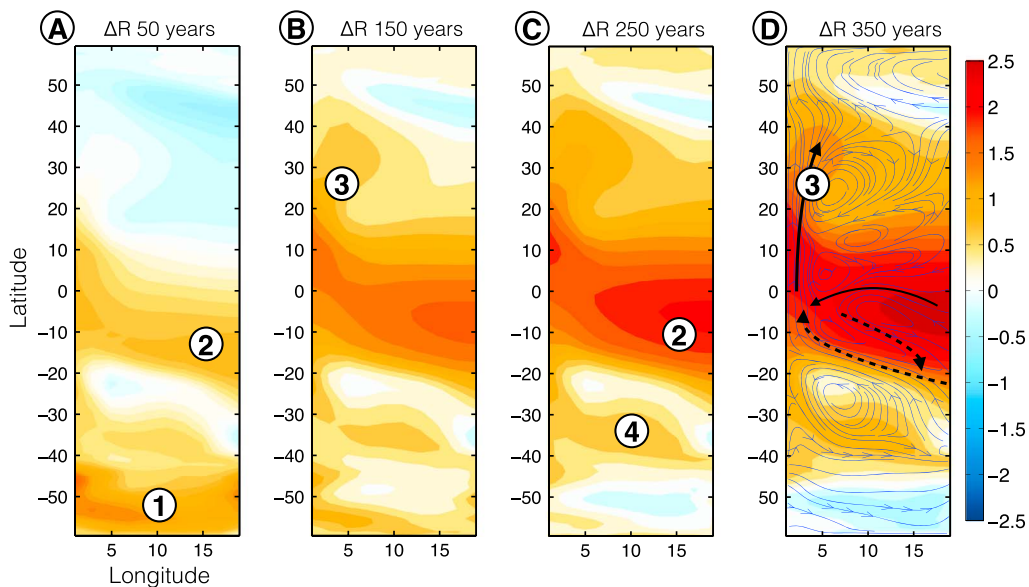
Figure 8. Revelle buffer factor anomaly ($2 \times \tau_{SO}$, control) along the perturbed $\sigma_\theta = 26$ kg/m^3 surface after (a) 50, (b) 150, (c) 250, and (d) 400 years. The blue arrows in Figure 8d show the perturbed flow field along the σ'_{26} surface. The black arrows show the primary advection pathway out of the equatorial shadow zone, while the dashed arrows show a secondary advection pathway due to recirculation within the shadow zone.

zone itself is present, leading to further advection toward the southern edge of the shadow zone. After the R anomaly is entrained into the nutrient stream, it follows the MOC transport northward (region 3) into the subtropical gyre where it is upwelled into the surface. The positive R anomaly in the intermediate waters just north of the Southern Ocean, denoted by region 4 in Figure 8c, is only 10% to 30% of the equatorial signal since the intermediate waters are ventilated at the surface prior to subduction.

4.3. Verification of the Mechanism
The effects of Southern Ocean mixing and nutrient export on low- and high-latitude biological productivity have been extensively studied [*Anderson et al.*, 2002; *Sarmiento et al.*, 2004; *Marinov et al.*, 2006]. However, the

Figure 9. Passive dye tracer along the unperturbed $\sigma_\theta = 26$ kg/m^3 surface after (a) 0, (b) 10, and (c) 20 years in an unperturbed control simulation.

Figure 10. (a) Change in $\overline{R_{na}}$ as a function of $\frac{\overline{F_{bio,eq}}}{\overline{F_{bio,na}}}$ calculated from experiments with wind stress perturbations alone (black squares), wind stress alone in the 40° longitude mo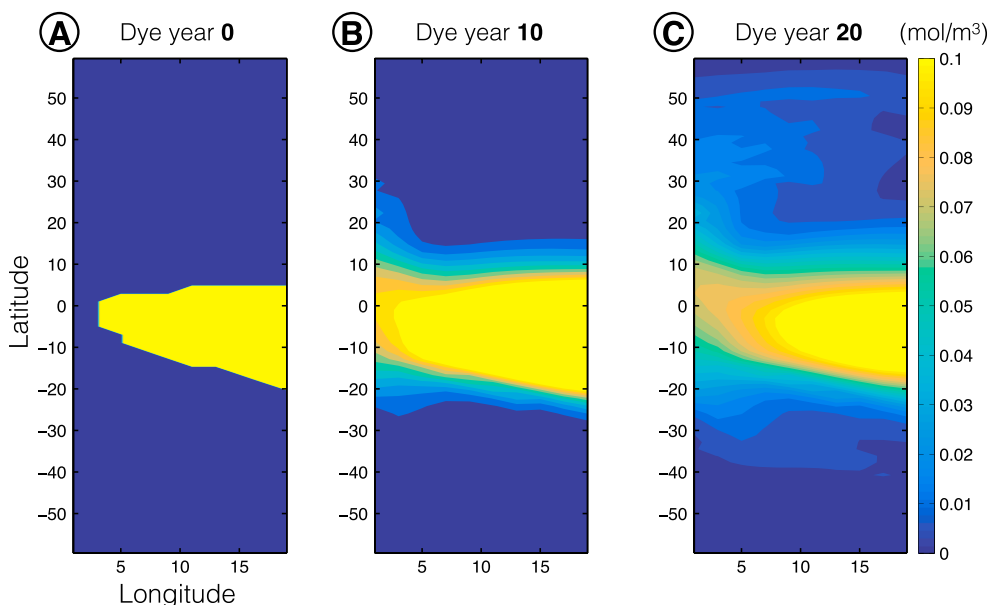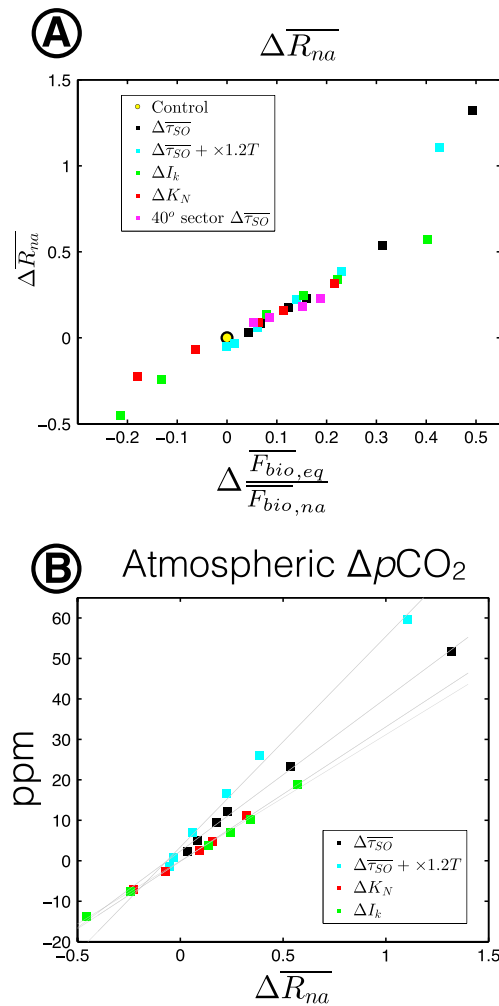del (magenta), wind stress and temperature perturbations (cyan squares), light half-saturation constant perturbations (green squares), and nutrient half-saturation constant perturbations (red squares). (b) Change in pCO_2^a as a function of $\Delta\overline{R_{na}}$ (legend as in Figure 10a).

advective pathways of biogeochemical tracers from the equatorial shadow zone to the North Atlantic and their impact on the subpolar gyre buffer factor are fairly novel. Therefore, we run an additional experiment in which we release a passive dye tracer into the shadow zone along σ'_{26} where concentrations of oxygen are less than $0.17 mol/m^3$ in the control simulation (the oxygen-minimum zone). Figure 9a shows the initial distribution of the tracer along σ'_{26}, while Figures 9b and 9c show the dye concentration after 10 and 20 years, respectively. The tracer is being entrained near the western boundary and advected northward toward the subpolar gyre, where it is then mixed into the surface ocean. The advective time scale from the shadow zone to the North Atlantic subpolar gyre is roughly 15 years.

Figures 8 and 9 show that the positive R anomaly from the shadow zone is advected to the North Atlantic subpolar gyre. As discussed earlier, increases in surface biological activity in the subpolar gyre can reduce the local mixed layer buffer factor. However, by the time the enhanced nutrient stream reaches the subpolar gyre it is nearly stripped of the nutrient surplus so that the increase in biological activity in the North Atlantic subpolar gyre is not sufficient to reduce the positive R anomaly of the upwelled waters. The result is therefore an increase in the North Atlantic subpolar gyre buffer factor due to the increased Southern Ocean wind stress.

Following this argument, the net change in the North Atlantic buffer factor $\overline{R_{na}}$ should depend on the relative change in the ratio of equatorial and North Atlantic biological productivity, such that

$$\overline{R_{na}} \propto \frac{\overline{F_{bio,eq}}}{\overline{F_{bio,na}}}, \tag{6}$$

where the overbar refers to the spatial averages between 10°S and 10°N for the subscript "eq" and between 40° and 60°N for the subscript "na." Since an increase in the buffer factor $\overline{R_{na}}$ reduces the capacity of the North Atlantic to absorb atmospheric CO_2, we also expect that the atmospheric pCO_2 will scale with $\overline{R_{na}}$ such that

$$pCO_2^a \propto \overline{R_{na}}. \tag{7}$$

Using the MITgcm numerical simulations in which the wind stress is perturbed, we will explore the validity of equations (6) and (7). We run further simulations to explore the sensitivity of the results using wind stress perturbation experiments with a warmed spin-up state, with increased ocean stratification. The model is warmed by increasing the temperature restoring profile shown in Figure 1c by 30% across the domain. The warmed model reaches a new equilibrium after 3000 years, at which time we introduce the same Southern Ocean wind stress perturbations described in section 2.2, up to a $3 \times \tau_{SO}$ perturbation.

Furthermore, experiments were also run whereby only the biogeochemical component in MITgcm is perturbed while keeping the wind stress profile constant. The parameters altered are the nutrient limitation

half-saturation constant K_N [*Monod*, 1949] and the light limitation half-saturation constant I_k [*Jassby and Platt*, 1976]. The effect of perturbing the biogeochemical component is to increase or decrease biological activity by an amount which depends on the local light or nutrient limitation, without affecting the circulation so that the changes seen in $\overline{F_{bio,eq}}$ and $\overline{F_{bio,na}}$ are purely biogeochemical. Increasing K_N causes areas that were not limited in macronutrients (e.g., high latitudes) to become limited, effectively increasing $\frac{\overline{F_{bio,eq}}}{\overline{F_{bio,na}}}$. On the other hand, an increasing I_k reduces light limitation more at high latitudes compared to the tropics, giving a reduction in $\frac{\overline{F_{bio,eq}}}{\overline{F_{bio,na}}}$. The nutrient and light half-saturation perturbation experiments are designed to show that an increase in atmospheric pCO$_2$ can also be caused by perturbations in the biology due to factors other than wind stress. The proposed feedback mechanism is therefore not solely dependent on Southern Ocean wind stress but can be caused by other climate change-induced factors that affect surface biological activity, such as freshwater or micronutrient input.

The results for all numerical experiments to test equations (6) and (7) are shown in Figure 10. Figure 10a shows that changes in $\frac{\overline{F_{bio,eq}}}{\overline{F_{bio,na}}}$ induce a linear change in $\overline{R_{na}}$ relative to the control state, $\Delta\overline{R_{na}}$, following the prediction of equation (6). The relationship is linear for perturbations less than 60% of the mean state. Furthermore, Figure 10b shows that ΔpCO$_2^a$ varies linearly with $\Delta\overline{R_{na}}$ as predicted, where Δ indicates again the anomaly relative to the control state. The sensitivity of the atmospheric pCO$_2^a$ anomaly to changes in the North Atlantic buffer factor in Figure 10b depends on the control value of pCO$_2^o$ and DIC concentration values, explaining the different slopes. The MITgcm experiments therefore show that an increase in tropical biological activity relative to northern subpolar gyre biological activity results in an increase in atmospheric pCO$_2$, under a variety of wind stress and biogeochemical forcing scenarios.

5. Conclusion and Discussion

5.1. Summary of Findings

The goal of this paper is to quantify the nonlocal equilibrium climate feedback of Southern Ocean wind stress on atmospheric pCO$_2$, pCO$_2^a$, using idealized coarse-resolution MITgcm experiments. In addition to triggering local changes in the Southern Ocean, an increase in the westerlies over the Southern Ocean can lead to changes in the biogeochemical and dynamical quantities in the Northern Hemisphere. Primarily, the North Atlantic carbon sink is found to be reduced several decades after an increase in Southern Ocean winds. The resulting feedback on atmospheric pCO$_2$, measured by the nonlocal feedback parameter ϵ, is of roughly the same order as the local Southern Ocean feedback. Overall, the nonlocal effect of Southern Ocean wind stress perturbations on atmospheric pCO$_2$ magnifies the local effect by 80% to 110%. The reduction in the North Atlantic carbon sink therefore constitutes a significant climate feedback that cannot be measured by considering changes in the Southern Ocean carbon sink alone.

Driving the reduction in the North Atlantic carbon sink is an increase in the Revelle buffer factor. It is found that wind stress-induced upwelling strengthens the export of nutrients north of the Southern Ocean by increasing the nutrient stream and increases equatorial biological productivity. The increased equatorial biological productivity increases the Revelle buffer factor, R, in the eastern tropical shadow zone/oxygen-minimum zone located between 100 and 700m depth. Via ocean interior advective pathways, the waters enriched in R are entrained into the nutrient stream and transported to the North Atlantic where they are inducted into the seasonal thermocline, increasing the subpolar gyre buffer factor and ocean pCO$_2$, pCO$_2^o$. Due to the reduction in the North Atlantic carbon sink, atmospheric pCO$_2$ is increased. The mechanism is also verified by only perturbing the biogeochemical component of the model.

5.2. Caveats and Implications

The use of a coarse-resolution model introduces several caveats. Coarse-resolution models fail to accurately represent the extent of the oxygen-minimum zones. Due to the unresolved complexity in equatorial undercurrents, a phenomenon coined "nutrient trapping" [*Najjar*, 1990; *Aumont et al.*, 1999] results in overestimation of the strength of the oxygen minimum in the tropics. Nonetheless, the proposed mechanism should still be valid since oxygen-minimum zones are observed in the ocean [*Stramma et al.*, 2009]. However, nutrient trapping could amplify the strength of the nonlocal feedback due to an exaggerated biogeochemical response in the tropics. Unresolved eddies in the Southern Ocean also overestimate the wind stress-induced increase in nutrient upwelling, since a constant Gent-McWilliams coefficient is used in the model. However, both Southern Ocean pCO$_2^o$ and the relative response of the North Atlantic and equatorial biology depend equally

on upwelling in the Southern Ocean so we do not expect this to affect the relative magnitude of the nonlocal feedback, although it may affect the equilibration time scale. For a full appreciation of the effect of eddies, a high-resolution eddy-permitting or eddy-resolving simulation is required.

Lastly, the geometry of the sector model introduces several caveats: the size of the basin plays an important role in setting the equilibration time scale of the nonlocal Southern Ocean winds feedback on pCO_2^a. The feedback equilibration time scale depends on basin-wide advection: the buffer factor anomaly in the shadow zone has to be advected zonally from east to west across a larger oxygen-minimum zone before it is advected northward by the nutrient steam. To illustrate this dependence of the time scale on basin width, an identical MITgcm setup 40° wide in longitude is used where the equilibration takes twice as long in the 40° longitude model (see supporting information). However, the strength of the nonlocal feedback ϵ is similar. The width of the basin therefore determines the time scale of the nonlocal feedback but not the magnitude. Further study is required to determine the exact equilibration time scale with a realistic geometry. The model also lacks a Pacific Ocean and Indian Ocean. However, the lack of MOC-like large-scale overturning transport and lack of strong ocean carbon uptake in the Pacific and Indian basins means that the presence of these basins will not affect the magnitude of the feedback of Southern Ocean winds on atmospheric CO_2 via the North Atlantic subpolar gyre. The increase in biological carbon drawdown in the Pacific and Indian basins as a result of increased nutrient transport is likely to be small due to the simultaneous input of surface carbon.

The relationship between the North Atlantic buffer factor and equatorial biology has further implications for the climate as well, since the ratio of North Atlantic to equatorial biology can be altered by many processes such as stratification, cloud cover, other sources of macronutrients, and iron supply, to name a few. Our results show the influence of oxygen-minimum zones on North Atlantic surface chemistry. Given recent results from studies that show expansion of tropical oxygen-minimum zones [*Stramma et al.*, 2012], a thorough understanding of the biogeochemical drivers of the North Atlantic buffer factor is therefore needed. The North Atlantic subpolar region constitutes one of the main sinks for anthropogenic CO_2, and our results show that changes in the buffer factor of as small as 0.5 could result in a positive atmospheric carbon feedback of 10–30ppm.

Furthermore, Southern Ocean winds and vertical mixing have been used to partially explain glacial-interglacial cycles of atmospheric CO_2. *Francois et al.* [1997] and *Anderson et al.* [2009] suggest that there was an increase in vertical mixing in the Southern Ocean at the end of the Last Glacial Maximum (LGM), 20,000–12,000 years B.P., possibly related to an increase in wind stress. So far, however, current theories of physical mechanisms have not been able to fully explain the glacial-interglacial cycles of atmospheric CO_2 [*Sigman and Boyle*, 2000; *Solomon*, 2007]. Including the effects of the nonlocal atmospheric feedback of the North Atlantic due to Southern Ocean vertical mixing could aid our understanding of glacial-interglacial atmospheric CO_2 cycles.

Kohfeld et al. [2005] show that there was higher biological carbon export in the Atlantic equatorial shadow zone in the LGM but states that "these areas are relatively small and do not affect the overall picture," while our research shows that these areas should not be overlooked. Although global changes in ocean alkalinity have been acknowledged as being potentially important, there has been no consideration of spatial patterns. *Kohfeld et al.* [2005] does not give exact figures of the relative change in biological export in the tropics and North Atlantic. However, *Francois et al.* [1997] suggest that Southern Ocean vertical mixing was increased by 20% to 50% at the end of the LGM, which, given our model study, would correspond to an increase in atmospheric pCO_2 of 15–35ppm in addition to the local Southern Ocean outgassing.

References

Anderson, L., and J. Sarmiento (1994), Redfield ratios of remineralization determined by nutrient data-analysis, *Global Biogeochem. Cycles*, *8*(1), 65–80, doi:10.1029/93GB03318.

Anderson, R., Z. Chase, M. Fleisher, and J. Sachs (2002), The Southern Ocean's biological pump during the Last Glacial Maximum, *Deep Sea Res., Part II*, *49*(9–10), 1909–1938, doi:10.1016/S0967-0645(02)00018-8.

Anderson, R. F., S. Ali, L. I. Bradtmiller, S. H. H. Nielsen, M. Q. Fleisher, B. E. Anderson, and L. H. Burckle (2009), Wind-driven upwelling in the Southern Ocean and the deglacial rise in atmospheric CO_2, *Science*, *323*(5920), 1443–1448, doi:10.1126/science.1167441.

Aumont, O., J. Orr, P. Monfray, G. Madec, and E. Maier-Reimer (1999), Nutrient trapping in the equatorial Pacific: The ocean circulation solution, *Global Biogeochem. Cycles*, *13*(2), 351–369.

Boyd, P. W., et al. (2000), A mesoscale phytoplankton bloom in the polar Southern Ocean stimulated by iron fertilization, *Nature*, *407*, 695–702.

Bracegirdle, T. J., E. Shuckburgh, J.-B. Sallee, Z. Wang, A. J. S. Meijers, N. Bruneau, T. Phillips, and L. J. Wilcox (2013), Assessment of surface winds over the Atlantic, Indian, and Pacific Ocean sectors of the Southern Ocean in CMIP5 models: Historical bias, forcing response, and state dependence, *J. Geophys. Res. Atmos.*, *118*, 547–562, doi:10.1002/jgrd.50153.

Brandt, P., et al. (2015), On the role of circulation and mixing in the ventilation of oxygen minimum zones with a focus on the eastern tropical North Atlantic, *Biogeosciences*, *12*(2), 489–512, doi:10.5194/bg-12-489-2015.

Coale, K. H., et al. (2004), Southern Ocean iron enrichment experiment: Carbon cycling in high- and low-SI waters, *Science*, *304*, 408–414.

DeVries, T., F. Primeau, and C. Deutsch (2012), The sequestration efficiency of the biological pump, *Geophys. Res. Lett.*, *39*, L13601, doi:10.1029/2012GL051963.

Dickson, R. R., J. Meincke, and P. Rhines (2008), *Arctic-Subarctic Ocean Fluxes: Defining the Role of the Northern Seas in Climate*, Springer, Netherlands.

Dutkiewicz, S., M. Follows, and P. Parekh (2008), Interactions of the iron and phosphorus cycles: A three-dimensional model study, *Global Biogeochem. Cycles*, *19*, GB1021, doi:10.1029/2004GB002342.

Emerson, S., C. Sabine, M. F. Cronin, R. Feely, S. E. C. Gray, and M. DeGrandpre (2011), Quantifying the flux of $CaCO_3$ and organic carbon from the surface ocean using in situ measurements of O_2, N_2, pCO_2, and pH, *Global Biogeochem. Cycles*, *25*, GB3008, doi:10.1029/2010GB003924.

Feely, R. A., C. L. Sabine, T. Takahashi, and R. Wanninkhof (2001), Uptake and storage of carbon dioxide in the oceans: The global CO_2 survey, *Oceanography*, *14*, 18–32.

Firing, E., S. Wijffels, and P. Hacker (1998), Equatorial subthermocline currents across the Pacific, *J. Geophys. Res.*, *103*(C10), 21,413–21,423, doi:10.1029/98JC01944.

Follows, M. J., T. Ito, and S. Dutkiewicz (2006), On the solution of the carbonate chemistry system in ocean biogeochemistry models, *Ocean Modell.*, *12*, 290–301.

Francois, R., M. Altabet, E. Yu, D. Sigman, M. Bacon, M. Frank, G. Bohrmann, G. Bareille, and L. Labeyrie (1997), Contribution of Southern Ocean surface-water stratification to low atmospheric CO_2 concentrations during the last glacial period, *Nature*, *389*(6654), 929–935, doi:10.1038/40073.

Gent, P., and J. McWilliams (1990), Isopycnal mixing in ocean circulation models, *J. Phys. Oceanogr.*, *20*, 150–160.

Gnanadesikan, A. (1999), A simple predictive model for the structure of the oceanic pycnocline, *Science*, *283*(5410), 2077–2079, doi:10.1126/science.283.5410.2077.

Group, T. L. S. (1998), The Labrador Sea deep convection experiment, *Bull. Am. Meteorol. Soc.*, *79*, 2033–2058.

Gruber, N. (1998), Anthropogenic CO_2 in the Atlantic Ocean, *Global Biogeochem. Cycles*, *12*, 256–270.

Halloran, P. R., B. B. B. Booth, C. D. Jones, F. H. Lambert, D. J. McNeall, I. J. Totterdell, and C. Voelker (2015), The mechanisms of North Atlantic CO_2 uptake in a large Earth System Model ensemble, *Biogeosciences*, *12*, 4497–4508.

Ito, T., and M. J. Follows (2003), Upper ocean control on the solubility pump of CO_2, *J. Mar. Res.*, *61*, 465–489.

Ito, T., and M. J. Follows (2005), Preformed phosphate, soft tissue pump and atmospheric CO_2, *J. Mar. Res.*, *63*, 813–839.

Ito, T., M. Woloszyn, and M. Mazloff (2010), Anthropogenic carbon dioxide transport in the Southern Ocean driven by Ekman flow, *Nature*, *463*(7277), 80–85, doi:10.1038/nature08687.

Izumo, T., J. Picaut, and B. Blanke (2002), Tropical pathways, equatorial undercurrent variability and the 1998 La Nina, *Geophys. Res. Lett.*, *29*(22), 2080, doi:10.1029/2002GL015073.

Jassby, A., and T. Platt (1976), Mathematical formulation of relationship between photosynthesis and light for phytoplankton, *Limnol. Oceanogr.*, *21*(4), 540–547.

Jin, X., N. Gruber, J. P. Dunne, J. L. Sarmiento, and R. A. Armstrong (2006), Diagnosing the contribution of phytoplankton functional groups to the production and export of particulate organic carbon, $CaCO_3$, and opal from global nutrient and alkalinity distributions, *Global Biogeochem. Cycles*, *20*, GB2015, doi:10.1029/2005GB002532.

Key, R., A. Kozyr, C. Sabine, K. Lee, R. Wanninkhof, J. Bullister, R. Feely, F. Millero, C. Mordy, and T. Peng (2004), A global ocean carbon climatology: Results from Global Data Analysis Project (GLODAP), *Global Biogeochem. Cycles*, *18*, GB4031, doi:10.1029/2004GB002247.

Khatiwala, S., F. Primeau, and T. Hall (2009), Reconstruction of the history of anthropogenic CO_2 concentrations in the ocean, *Nature*, *462*, 346–349.

Kieke, D., and I. Yashayaev (2014), Studies of Labrador Sea water formation and variability in the subpolar North Atlantic in the light of international partnership and collaboration, *Prog. Oceanogr.*, *79*, 220–232.

Knauss, J. (1960), Measurements of the Cromwell Current, *Deep Sea Res.*, *6*(4), 265–286.

Kohfeld, K., C. Le Quere, S. Harrison, and R. Anderson (2005), Role of marine biology in glacial-interglacial CO_2 cycles, *Science*, *308*(5718), 74–78, doi:10.1126/science.1105375.

Lauderdale, J. M., A. C. N. Garabato, K. I. C. Oliver, M. J. Follows, and R. G. Williams (2013), Wind-driven changes in Southern Ocean residual circulation, ocean carbon reservoirs and atmospheric CO_2, *Clim. Dyn.*, *41*(7–8), 2145–2164, doi:10.1007/s00382-012-1650-3.

Le Quere, C., et al. (2007), Saturation of the Southern Ocean CO_2 sink due to recent climate change, *Science*, *316*, 1735–1738.

Lovenduski, N., and T. Ito (2009), The future evolution of the Southern Ocean CO_2 sink, *J. Mar. Res.*, *67*, 597–617.

Lovenduski, N. S., N. Gruber, S. C. Doney, and I. D. Lima (2007), Enhanced CO_2 outgassing in the Southern Ocean from a positive phase of the Southern Annular Mode, *Global Biogeochem. Cycles*, *21*, GB2026, doi:10.1029/2006GB002900.

Lovenduski, N. S., N. Gruber, and S. C. Doney (2008), Toward a mechanistic understanding of the decadal trends in the Southern Ocean carbon sink, *Global Biogeochem. Cycles*, *22*, GB3016, doi:10.1029/2007GB003139.

Marinov, I., A. Gnanadesikan, J. Toggweiler, and J. Sarmiento (2006), The Southern Ocean biogeochemical divide, *Nature*, *441*(7096), 964–967, doi:10.1038/nature04883.

Marshall, J., and T. Radko (2003), Residual-mean solutions for the antarctic circumpolar current and its associated overturning circulation, *J. Phys. Oceanogr.*, *33*, 2341–2354.

Marshall, J., and K. Speer (2012), Closure of the meridional overturning circulation through Southern Ocean upwelling, *Nat. Geosci.*, *5*(3), 171–180, doi:10.1038/NGEO1391.

Marshall, J., A. Adcroft, C. Hill, L. Perelman, and C. Heisey (1997), A finite-volume, incompressible Navier Stokes model for studies of the ocean on parallel computers, *J. Geophys. Res.*, *102*, 5753–5766.

Monod, J. (1949), The growth of bacterial cultures, *Annu. Rev. Microbiol.*, *3*, 371–394, doi:10.1146/annurev.mi.03.100149.002103.

Munday, D. R., H. L. Johnson, and D. P. Marshall (2013), Eddy saturation of equilibrated circumpolar currents, *J. Phys. Oceanogr.*, *43*, 507–532.

Munday, D. R., H. L. Johnson, and D. P. Marshall (2014), Impacts and effects of mesoscale ocean eddies on ocean carbon storage and atmospheric pCO_2, *Global Biogeochem. Cycles*, *28*, 877–896, doi:10.1002/2014GB004836.

Najjar, R. G. (1990), Simulations of the phosphorus and oxygen cycles in the world ocean using a general circulation model, PhD thesis, Princeton, N. J.

Nielsdottir, M. C., C. M. Moore, R. Sanders, D. J. Hinz, and E. P. Achterberg (2009), Iron limitation of the postbloom phytoplankton communities in the Iceland Basin, *Global Biogeochem. Cycles*, *23*, GB3001, doi:10.1029/2008GB003410.

Palter, J. B., J. L. Sarmiento, A. Gnanadesikan, J. Simeon, and R. D. Slater (2010), Fueling export production: Nutrient return pathways from the deep ocean and their dependence on the meridional overturning circulation, *Biogeosciences*, *7*(11), 3549–3568, doi:10.5194/bg-7-3549-2010.

Pelegri, J. L., and G. T. Csanady (1991), Nutrient transport and mixing in the gulf stream, *J. Geophys. Res.*, *96*, 2577–2583.

Pelegri, J. L., G. T. Csanady, and A. Martins (1996), The North Atlantic nutrient stream, *J. Oceanogr.*, *52*, 275–299.

Pelegri, J. L., A. MArrero-Diaz, and A. W. Ratsimandresy (2006), Nutrient irrigation of the North Atlantic, *Prog. Oceanogr.*, *70*, 366–406.

Philander, S. (1973), Equatorial undercurrent—Measurements and theories, *Rev. Geophys.*, *11*(3), 513–570, doi:10.1029/RG011i003p00513.

Philander, S., W. Hurlin, and A. Seigel (1987), Simulation of the seasonal cycle of the tropical Pacific Ocean, *J. Phys. Oceanogr.*, *17*(11), 1986–2002, doi:10.1175/1520-0485(1987)017<1986:SOTSCO>2.0.CO;2.

Qiu, B., D. L. Rudnick, S. Chen, and Y. Kashino (2013), Quasi-stationary north equatorial undercurrent jets across the tropical North Pacific Ocean, *Geophys. Res. Lett.*, *40*, 2183–2187, doi:10.1002/grl.50394.

Redfield, A. (1934), On the proportions of organic derivatives in sea water and their relation to the composition of plankton, in *James Johnstone Memorial Volume*, edited by R. J. Daniel, pp. 177–192, Univ. Press of Liverpool, Liverpool, U. K.

Revelle, R., and H. S. Suess (1957), Carbon dioxide exchange between atmosphere and ocean and the questions of an increase of atmospheric CO_2 during the past decades, *Tellus*, *9*, 18–27.

Rowe, G., E. Firing, and G. Johnson (2000), Pacific equatorial subsurface countercurrent velocity, transport, and potential vorticity, *J. Phys. Oceanogr.*, *30*(6), 1172–1187, doi:10.1175/1520-0485(2000)030<1172:PESCVT>2.0.CO;2.

Sarmiento, J., J. Dunne, A. Gnanadesikan, R. Key, K. Matsumoto, and R. Slater (2002), A new estimate of the CaCO3 to organic carbon export ratio, *Global Biogeochem. Cycles*, *16*(4), 1107, doi:10.1029/2002GB001919.

Sarmiento, J. L., N. Gruber, M. A. Brzezinski, and J. P. Dunne (2004), High-latitude controls of thermocline nutrients and low latitude biological productivity, *Nature*, *427*, 56–60.

Sigman, D., and E. Boyle (2000), Glacial/interglacial variations in atmospheric carbon dioxide, *Nature*, *407*(6806), 859–869, doi:10.1038/35038000.

Solomon, S. (2007), *Climate Change 2007—The Physical Science Basis: Working Group I Contribution to the Fourth Assessment Report of the IPCC*, vol. 4, Cambridge Univ. Press, Cambridge, U. K.

Stramma, L., M. Visbeck, P. Brandt, T. Tanhua, and D. Wallace (2009), Deoxygenation in the oxygen minimum zone of the eastern tropical North Atlantic, *Geophys. Res. Lett.*, *36*, L20607, doi:10.1029/2009GL039593.

Stramma, L., E. D. Prince, S. Schmidtko, J. Luo, J. P. Hoolihan, M. Visbeck, D. W. R. Wallace, P. Brandt, and A. Koertzinger (2012), Expansion of oxygen minimum zones may reduce available habitat for tropical pelagic fishes, *Nat. Clim. Change*, *2*(1), 33–37, doi:10.1038/NCLIMATE1304.

Swart, N. C., J. C. Fyfe, O. A. Saenko, and M. Eby (2014), Wind-driven changes in the ocean carbon sink, *Biogeosciences*, *11*, 6107–6117.

Takahashi, T., et al. (2009), Climatological mean and decadal change in surface ocean pCO$_2$ and net sea-air co2 flux over the global oceans, *Deep Sea Res., Part II*, *56*, 554–577.

Tsuchiya, M. (1972), Subsurface North Equatorial Countercurrent in eastern Pacific Ocean, *J. Geophys. Res.*, *77*(30), 5981–5986, doi:10.1029/JC077i030p05981.

Valsala, V., and S. Maksyutov (2010), Simulation and assimilation of global ocean pCO$_2$ and air-sea CO$_2$ fluxes using ship observations of surface ocean pCO$_2$ in a simplified biogeochemical offline model, *Tellus B*, *62*(5), 821–840, doi:10.1111/j.1600-0889.2010.00495.x.

Wanninkhof, R. (1992), Relationship between wind speed and gas exchange over the ocean, *J. Geophys. Res.*, *97*, 7373–7382.

Weber, T., and C. Deutsch (2012), Oceanic nitrogen reservoir regulated by plankton diversity and ocean circulation, *Nature*, *489*, 419–422.

Williams, R., and M. Follows (1998), The Ekman transfer of nutrients and maintenance of new production over the North Atlantic, *Deep Sea Res., Part I*, *45*(2–3), 461–489, doi:10.1016/S0967-0637(97)00094-0.

Williams, R. G., and M. Follows (2011), *Ocean Dynamics and the Carbon Cycle: Principles and Mechanics*, Cambridge Univ. Press, Cambridge, U. K.

Williams, R. G., V. Roussenov, and M. J. Follows (2006), Nutrient streams and their induction into the mixed layer, *Global Biogeochem. Cycles*, *20*, GB1016, doi:10.1029/2005GB002586.

Williams, R. G., E. McDonagh, V. Roussenov, S. Torres-Valdes, B. King, R. Sanders, and D. A. Hansel (2011), Nutrient streams in the North Atlantic: Advective pathways of inorganic and dissolved organic nutrients, *Global Biogeochem. Cycles*, *25*, GB4008, doi:10.1029/2010GB003853.

Wolfe, C., and P. Cessi (2010), What sets the strength of the midddepth stratification and overturning circulation in eddying ocean models?, *J. Phys. Oceanogr.*, *40*, 1520–1538.

Wyrtki, K., and B. Kilonsky (1984), Mean water and current structure during the Hawaii-To-Tahiti shuttle experiment, *J. Phys. Oceanogr.*, *14*(2), 242–254, doi:10.1175/1520-0485(1984)014<0242:MWACSD>2.0.CO;2.

Supporting Information for 'The Influence of Southern Ocean Winds on the North Atlantic Carbon Sink"

Ben Bronselaer[1], Laure Zanna[1] David R. Munday[1,2], and Jason Lowe[3]

Here we present a detailed derivation of the non-local feedback parameter and atmospheric feedback equation described in the main paper. In addition, we present data from a Southern Ocean wind stress perturbation experiment performed with an identical MITgcm set-up as used in the main paper, but 40° in longitude.

————

Corresponding author: B. Bronselaer, Atmospheric, Oceanic and Planetary Physics, Department of Physics, University of Oxford, Oxford, OX1 3PU, UK. (benjamin.bronselaer@physics.ox.ac.uk)

[1]Atmospheric, Oceanic and Planetary

Physics, Department of Physics, University

of Oxford, Oxford, OX1 3PU, UK.

[2] British Antarctic Survey, Madingley

Road, Cambridge, CB3 0ET, UK

[3]Met Office Hadley Centre, FitzRoy

Road, Exeter, Devon EX1 3PB, UK

The value of oceanic pCO_2, pCO_2^o, as a function of a forcing τ, $pCO_2^o(\tau)$ is obtained by using the equation for global air-sea carbon flux, $F_{air-sea}$, in the absence of anthropogenic carbon emissions. At equilibrium, the globally area integrated flux over the whole ocean vanishes such that:

$$\int F_{air-sea} dA = \int K\tau(pCO_2^a - pCO_2^o(\tau))dA = 0, \tag{1}$$

where τ is proportional to the square of the wind speed. K measures the turbulent air-sea gas transfer and solubility such that $K\tau = k$, where k is the piston velocity of *Wanninkhof* [1992] which varies as the square of the surface wind speed. pCO_2^a is the atmospheric partial pressure of CO_2. We are interested in the Southern Ocean and North Atlantic pCO_2^o response to local forcing so we split the integral into a Southern Ocean area A_{SO} where the forcing τ is applied, the North Atlantic A_{NA} and the remaining area in the ocean, A_E (see Fig. S1):

$$\overline{\tau_{SO}pCO_{SO}^o(\tau)} + \overline{\tau_{NA}pCO_{NA}^o(\tau)} + A_E\overline{\tau_E pCO_{2E}^o}$$

$$- (A_{SO}\overline{\tau_{SO}} + A_{NA}\overline{\tau_{NA}} + A_E\overline{\tau_E})pCO_2^a = 0, \tag{2}$$

where the overline indicates an area-mean. Equation 2 can be solved for pCO_2^a to give pCO_2^a in terms of pCO_{SO}^o and pCO_{NA}^o. We approximate $\overline{\tau_{SO}pCO_{SO}^o(\tau)}$ by $\overline{\tau_{SO}}\,\overline{pCO_{SO}^o(\tau)}$ and similarly for the other terms, thereby introducing a constant error smaller than 3% in the model and regions used in this study. The feedback equation is then given by:

$$pCO_2^a = P_{SO}\overline{pCO_{SO}^o}(\tau) + P_{NA}\overline{pCO_{NA}^o}(\tau) + P_E\overline{pCO_{2E}^o}, \tag{3}$$

where $P_{SO} = \frac{A_{SO}\overline{\tau_{SO}}}{A_{SO}\overline{\tau_{SO}}+A_{NA}\overline{\tau_{NA}}+A_E\overline{\tau_E}}$ and similarly for P_{NA} and P_E. The proportionality term P_{SO} can be larger than A_{SO} in areas of high wind stress such as the Southern

Ocean, resulting in a strong influence of $\overline{pCO^o_{SO}(\tau)}$ on pCO^a_2. Since we are interested in atmospheric pCO_2 changes in response to a forcing τ, we express eqn. 3 in terms of perturbations to the equilibrium unperturbed state.:

$$\Delta pCO^a_2 = \quad \Delta P_{SO}\overline{pCO^o_{SO}} + P_{SO}\Delta\overline{pCO^o_{SO}(\tau)} + \Delta P_{NA}\overline{pCO^o_{NA}}$$
$$+ \quad P_{NA}\Delta\overline{pCO^o_{NA}(\tau)} + P_E\Delta\overline{pCO^o_{2E}(\tau)} + \Delta P_E\overline{pCO^o_{2E}}. \tag{4}$$

To account for the non-local effect of the forcing τ on $\overline{pCO^o_{2NA}}$, consider the box model shown in Fig. S1. The model is similar to that of *Toggweiler* [1999]. The model consists of an atmosphere of carbon concentration C_a and mass M_a that interacts with the surface ocean boxes in the Southern and Northern hemispheres with carbon concentrations C_{SO} and C_{NA}, and masses M_{SO} and M_{NA} through air-sea fluxes F_1 and F_2, respectively. Representing the overturning circulation, the volume transport Ψ connects the carbon concentrations C_{SO}, C_{NA} and a deep ocean with carbon concentration C_D. The carbon concentration in the South C_{SO} is further enriched through the overturning Ψ and a vertical mixing term. The mixing term is proportional to the difference $C_D - C_{SO}$ and depends on the strength of the mixing f. The forcing τ is applied to the Southern high latitude ocean and we interested in the subsequent change in C_{NA}. The region E between the Southern Ocean and North Atlantic is omitted because it serves no purpose other than simply transporting carbon from the Southern Ocean to the North Atlantic box through Ψ. The steady state transport of carbon in and out of the deep box is then given by

$$\Psi C_{NA} - \Psi C_D - f\left[C_D - C_{SO}\right] = 0, \tag{5}$$

such that the deep carbon concentration in steady state is:

$$C_D = (\Psi C_{NA} + f C_{SO}) (\Psi + f)^{-1}. \tag{6}$$

The upper ocean carbon concentration in the Northern box can be obtained by combining the previous expression with conservation of mass in the absence of carbon emissions, i.e. $M_A C_a + M_{NA} C_{NA} + M_{SO} C_{SO} + M_D C_D = I$, where I is the total carbon inventory, leading to

$$C_{NA} = \left[\frac{I}{M_D} - \frac{M_A}{M_D} C_a - C_{SO} \left(\frac{M_{SO}}{M_D} + \frac{f}{f + \Psi} \right) \right] \left(\frac{M_{NA}}{M_D} + \frac{\Psi}{f + \Psi} \right)^{-1}. \tag{7}$$

The atmospheric mass M_A is much less than the oceanic mass M_D and all the other terms apart from C_{SO} do not depend on carbon concentrations, so the expression for C_{NA} is of the form

$$C_{NA} = -\phi C_{SO} + c, \tag{8}$$

where c is a constant and ϕ is a function of f and Ψ, such that:

$$\phi = \left(\frac{M_{SO}}{M_D} + \frac{f}{f + \Psi} \right) \left(\frac{M_{NA}}{M_D} + \frac{\Psi}{f + \Psi} \right)^{-1}. \tag{9}$$

ϕ is only a function of positive quantities, so ϕ *is always positive*. From the relationship 8, C_{NA} is proportional to C_{SO}, coupled via the dynamical quantities f and Ψ. Therefore, if a forcing τ is applied over the Southern box and results in a local change in C_{SO}, ΔC_{SO}, there will be a non-local change in the carbon concentration C_{NA}, ΔC_{NA}, in the Northern box which is proportional to ΔC_{SO} such that:

$$\Delta C_{NA} = -\left(\phi \Delta C_{SO} + C_{SO} \frac{\Delta \phi}{\Delta C_{SO}} \Delta C_{SO} \right) = -\left(\phi \Delta C_{SO} + C_{SO} \frac{\Delta C_{SO}}{\Delta C_{SO}/\Delta \phi} \right). \tag{10}$$

To relate the changes in carbon concentration ΔC_{SO} and ΔC_{NA} to changes in mean ocean pCO_2, $\overline{pCO_{SO}^o}$ and $\overline{pCO_{2E}^o}$ respectively, we use the definition of the Buffer Factor R which

only holds for small perturbations in pCO_2^o:

$$\Delta pCO_2^o = R\frac{pCO_2^o}{C}\Delta C. \tag{11}$$

We take the spatial average of eqn. 11 separately:

$$\Delta\overline{pCO_{SO}^o} = \overline{R_{SO}\frac{pCO_{SO}^o}{C_{SO}}}\Delta\overline{C_{SO}}, \tag{12}$$

$$\Delta\overline{pCO_{2E}^o} = \overline{R_{NA}\frac{pCO_{2E}^o}{C_{NA}}}\Delta\overline{C_{NA}}, \tag{13}$$

where we have split the area integral on the right hand side to separate $\Delta\overline{C_{SO}}$ and $\Delta\overline{C_{NA}}$ in order to match these with C_{SO} and C_{NA} such that $\Delta\overline{C_{SO}} \equiv \Delta C_{SO}$ and $\Delta\overline{C_{NA}} \equiv \Delta C_{NA}$. Due to the small spatial variation of terms in eqns. 12 and 13, the error associated with this operation is less than 1% in all MITgcm experiments used in the main text. We can therefore write eqn. 10 as:

$$\Delta\overline{pCO_{2E}^o} = -\left(\phi + \overline{C_{SO}}\frac{\Delta\phi}{\Delta\overline{C_{SO}}}\right)\overline{R_{NA}\frac{pCO_{2E}^o}{C_{NA}}}\left(\overline{R_{SO}\frac{pCO_{SO}^o}{C_{SO}}}\right)^{-1}\Delta\overline{pCO_{SO}^o}, \tag{14}$$

$$\Delta\overline{pCO_{2E}^o} = \epsilon\Delta\overline{pCO_{SO}^o}. \tag{15}$$

The proportionality between $\Delta\overline{pCO_{2E}^o}$ and $\Delta\overline{pCO_{SO}^o}$ is expressed in terms of the parameter ϵ. The parameter ϵ is referred to as the non-local feedback parameter since it measures the influence of the local forcing τ on the pCO_2^o in rest of the ocean basin via non-local dynamical and biogeochemical induced changes. We can use the expression $\Delta\overline{pCO_{2E}^o} = \epsilon\Delta\overline{pCO_{SO}^o}$ to estimate the change in atmospheric pCO_2 due to the non-local feedback by substituting $\Delta\overline{pCO_{2E}^o}$ into eqn. 4 :

$$\Delta pCO_2^a = (1 + \epsilon\frac{P_E}{P_{SO}})P_{SO}\Delta\overline{pCO_{SO}^o} + \Delta P_{SO}\overline{pCO_{SO}^o} + \Delta P_{NA}\overline{pCO_{NA}^o} + \Delta P_E\overline{pCO_{2E}^o} \tag{16}$$

The size of the sector model plays an important role in setting the timescale of the non-local Southern Ocean winds feedback on $p\mathrm{CO}_2^a$. The feedback timescale depends on basin-wide advection: the Buffer Factor anomaly in the shadow zone has to be advected zonally from East to West before it is advected northwards by the nutrient steam. In a wider basin therefore, the cross-basin zonal advection timescale is longer. To illustrate this dependence of the timescale on basin width, an identical MITgcm set up 40° in longitude wide is used. Figure S3 shows the time evolution of atmospheric, Southern Ocean and North Atlantic sub-polar gyre $p\mathrm{CO}_2$ anomalies in $2 \times \tau_{SO}$ experiment for both the 20° and 40° wide models. While the non-local signal appears in the North Atlantic $p\mathrm{CO}_2^o$ after 20 years in each case, the equilibration timescales varies. After 500 years, atmospheric $p\mathrm{CO}_2$ has equilibrated in the 20° model while equilibration takes twice as long in the 40° longitude model. However, the strength of the non-local feedback ϵ is similar. The width of the basin therefore determines the timescale of the non-local feedback but not the magnitude. Further study is required to determine the exact equilibration timescale in a realistic bathymetry domain.

References

Toggweiler, J. (1999), Variation of atmospheric CO2 by ventilation of the ocean's deepest water, *Paleoceanography*, *14* (5), 571–588, doi:10.1029/1999PA900033.

Wanninkhof, R. (1992), Relationship between wind speed and gas exchange over the ocean, *Journal of Geophysical Research: Oceans*, *97*.
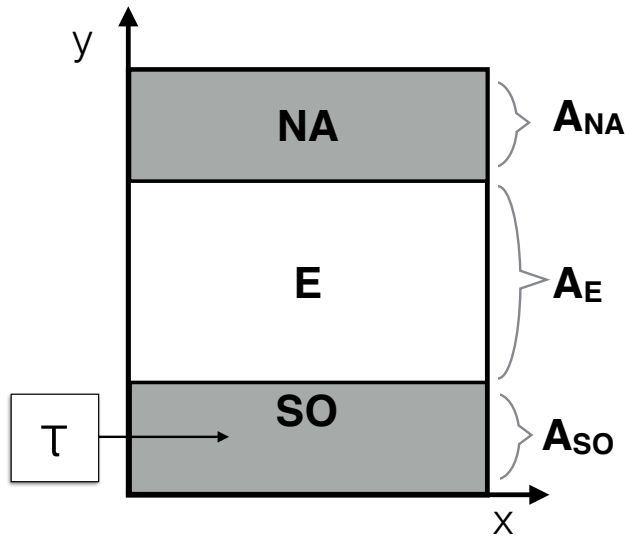
Figure S1. For a rectangular ocean basin shown, we label the Southern Ocean SO where we calculate the local response in pCO_{2SO}^o to a forcing τ, a region E where no forcing is applied and no change in pCO_{2E}^o occurs, and the North Atlantic NA where there is a non-local change in pCO_{2NA}^o.
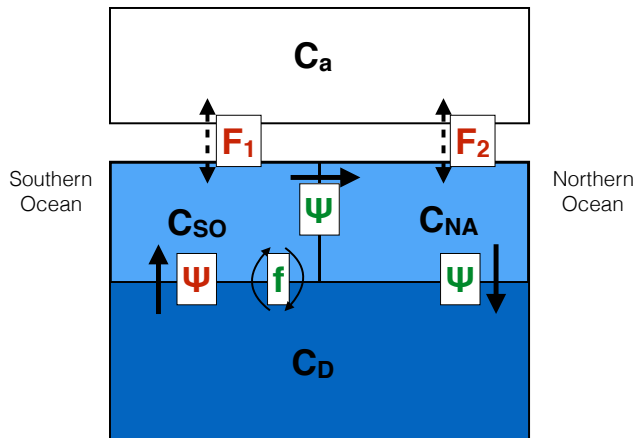
Figure S2. Simple box model adapted from *Toggweiler* [1999] with surface ocean boxes with carbon concentrations C_{SO} and C_{NA} over a deep ocean box with C_D and an atmosphere with C_a. F_1 and F_2 represent air-sea fluxes, Ψ is the overturning circulation and f represents vertical mixing

3.1.2. Southern Ocean carbon response

The response of the local ocean pCO_2 (pCO_2^o) to a change in temperature T can be quantified using an empirical relationship determined by Takahashi et al. [1993]:

$$\frac{\partial pCO_2^o}{\partial T} = 0.0423 \cdot pCO_2^o. \tag{3.2}$$

The relationship quantifies the ... as the temperature increases. The uncertainty ... $0.0423 \pm 0.0002°C^{-1}$ over a range ... Equation 3.2 is widely used ... (or biological) contributions in ... Maier et al., 2011, Roedenbeck ... 2014]. To estimate the change in ... surface temperature perturbation in ...

Figure S3. Time evolution of ΔpCO_2^a (black), North Atlantic $\overline{\Delta pCO_2^o}$ (red) and Southern ... Change in $\overline{pCO_2}$, in ppm, as a function of Southern channel sea surface temperature, equation 3.2. Here written ... A) the 20° longitude wide model and B) the 40° longitude wide model. Filled squares show MITgcm data from temperature perturbation experiments and the solid blue line is the prediction based solely on solubility effects.

$$\overline{\Delta pCO_2^o} = \langle \overline{pCO_2^o} \rangle e^{0.0423\overline{\Delta T}}, \tag{3.3}$$

While these results use an idealised ocean model, we believe the mechanisms discussed ...

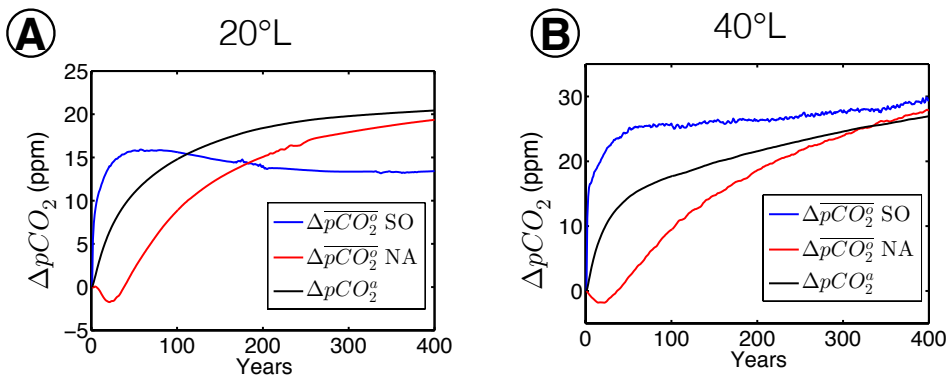... with $\overline{pCO_2^o}$ ... about 3.6 ... the difference is that the bottom water cell contains ... dynamical effects of solubility from other dynamical influences. So how well does equation 3.1.3 ... and based on solubility alone? ... The error between the prediction and the ... model the Southern Ocean response? Observations suggest that the bottom cell contains 1.7 times more ... is < 5% in all cases, such that the dynamical component is small. ... the upper cell [Johnson et al., 2008] whereas in the MITgcm model, the ... roughly 3. Since the observed bottom cell is much deeper and contains less ... temperature perturbation is applied to the ocean, it will result in ... the model equivalent, we expect that the dynamical effect of the warming ... and buoyancy and deepening of the pycnocline. Since transport is most ... be less than seen in the model, in which case the solubility effect is even ... ocean interior adiabatic in the ocean interior, the water that is upwelled in the Southern Ocean travels ... Additionally, since the ΔpCO_2^o depends largely on solubility, we do not ...

... upwelled therefore deepens as well and exposes more carbon-rich water ... setting the timescale of isopycnal adjustment [Gent and McWilliams, 1990, Allison et al. 2011].

... in the southern ocean weakens, the volume of water supplied reduces. However, ...